nature nanotechnology

Supplementary information

https://doi.org/10.1038/s41565-026-02142-z

Picosecond-scale coherent toggle switching of topological spin helicity

In the format provided by the authors and unedited

This file contains:

Supplementary Videos:

Supplementary Video 1 (.mov format). Analytical spin configuration of a magnetic vortex with evolution of the helicity angle $C\pi/2$.

Supplementary Video 2 (.mov format). Experimental observations of three types of helicity switching behaviors ($|\delta C| = 2, 1, 0$) in a circular Py disk in out-of-plane magnetic fields of 87, 99 and 131 mT, in each case in the presence of fs laser pulse excitation with a fluence of 19.5 mJ/cm^2.

Supplementary Video 3 (.mov format). Simulations of the three types of helicity switching behaviors ($|\delta C|$ = 2, 1, 0) in a circular Py disk in out-of-plane magnetic fields of 88, 100 and 126 mT, in each case in the presence of fs laser pulse excitation with a fluence of 19.5 mJ/cm^2. Upper panel: 3D (left panel) and top-down (right panel) views of the vortex helicity distribution during switching. Middle panel: Time evolution of the vortex helicity $\sin(C\pi/2)$. Lower panel: Trajectory of the vortex state on the Bloch sphere.

Supplementary Video 4 (.mov format). Simulations of alternative helicity switching behaviors in a circular Py disk in the presence of laser pulse excitation with fluences of 14.5, 16.3 and 19.5 mJ/cm^2 in an out-of-plane magnetic field of 163 mT. Upper panel: 3D (left panel) and top-down (right panel) views of the vortex helicity distribution during switching. Middle panel: Time evolution of the vortex helicity $\sin(C\pi/2)$. Lower panel: Trajectory of the vortex state on the Bloch sphere.

Supplementary Information

Note 1. Scaling of photothermal demagnetization curves for fs laser excitation of Py disks

The key prerequisite for performing fs-laser-induced dynamical micromagnetic simulations lies in establishing the interaction between the laser pulse and the magnetically-ordered permalloy (Py) disk. In general, light-matter interactions involve not only thermal but also nonthermal effects, such as the inverse Faraday and inverse Cotton-Mouton effects [1]. For thermal effects, the phenomenological 3TM is typically used to describe heat transfer between photon-excited electrons, spins and the lattice in the material. In the present work, we found that the polarization of light, whether linearly or circularly polarized, made no difference to the observed experimental phenomena, thereby ruling out nonthermal effects of the laser pulse. Instead, the laser fluence ($\leqslant$19.5 mJ/cm^2) has a strong impact on the helicity switching behavior of the magnetic vortex, indicating that photothermal demagnetization caused by thermal effects of the fs laser pulse plays a dominant role in the experiment. Considering that the focal spot size of the laser pulse (~120 μm) is much larger than the size of the Py disk (~1 μm), the behavior of the spontaneous magnetization $M_s(t)$ can be treated as homogeneous across the sample. As a result, the magnetization $M_s(T)$ after laser excitation will decrease uniformly with laser heating in the spin temperature $T = T_s(t)$, which determines the photothermal demagnetization curve $M_s(t)$. The phenomenological 3TM is therefore sufficient to simulate the interaction between the laser pulse and the magnetically-ordered Py disk.

To incorporate the 3TM into the LLG equation, a method has been developed for scaling the photothermal demagnetization curves $M_s(t)$ in micromagnetic systems. The time-dependent temperature evolution of the electron (T_e), spin (T_s) and lattice (T_l) subsystems has been simulated by employing the 3TM framework [2,3], enabling integration of laser-induced photothermal effects into micromagnetic simulations.

The temporal dynamics of the three subsystems are governed by the following coupled differential equations:

$$C_e(T_e)\frac{dT_e}{dt} = -G_{el}(T_e - T_l) - G_{es}(T_e - T_s) + P(t) \quad \text{(S1)}$$

$$C_s(T_s)\frac{dT_s}{dt} = -G_{es}(T_s - T_e) - G_{sl}(T_s - T_l) \quad \text{(S2)}$$

$$C_l(T_l)\frac{dT_l}{dt} = -G_{el}(T_l - T_e) - G_{sl}(T_l - T_s) \quad \text{(S3)}$$

where C_e, C_s, and C_l denote the heat capacities of the electron, spin and lattice subsystems, respectively, while G_{el}, G_{es} and G_{sl} represent the electron-lattice, electron-spin and spin-lattice coupling constants. For Py, the material-specific parameters have been selected from the reasonable ranges reported in previous references [4-7]. Within the physically reasonable literature ranges, we optimized the thermal

parameters (see **Table S1**) such that, for the laser fluences used in our experiments, the maximum spin temperature calculated within the 3TM remains close to, but does not exceed the Curie temperature.

Table S1| The parameters used for 3TM simulation. T is temperature in the unit of Kelvin (K).

Parameter	Value
C_e ($J \cdot m^{-3} \cdot K^{-1}$)	$700 \times T$
C_l ($J \cdot m^{-3} \cdot K^{-1}$)	4×10^6
C_s ($J \cdot m^{-3} \cdot K^{-1}$)	2.67×10^5
G_{el} ($J \cdot s^{-1} \cdot m^{-3} \cdot K^{-1}$)	2.6×10^{18}
G_{es} ($J \cdot s^{-1} \cdot m^{-3} \cdot K^{-1}$)	2.7×10^{17}
G_{ls} ($J \cdot s^{-1} \cdot m^{-3} \cdot K^{-1}$)	0

In the 3TM, the optical absorption coefficient under 515 nm laser excitation was experimentally determined to be approximately 0.3 using UV–vis spectroscopy. According to the optical energy conservation relation:

$$A + R + T = 1 \tag{S4}$$

where A, R, and T denote the absorption, reflection, and transmission coefficients, respectively. The result is illustrated in **Fig. S1**.

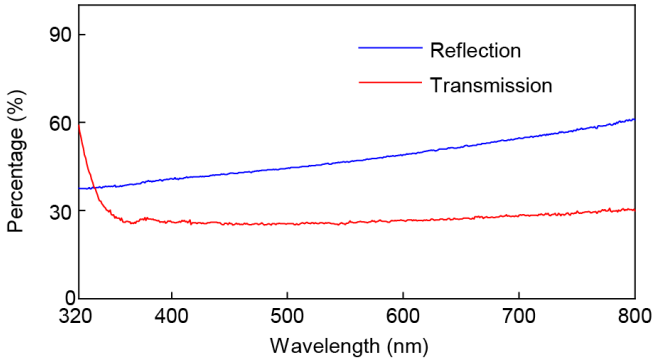

Fig. S1| Optical reflection and transmission spectra of the Py sample.

Based on the laser parameters and the coupling constants for Py [5,6], the 3TM solves the time-dependent T_e, T_s and T_l for laser fluences of between 15.0 and 19.5 mJ/cm^2 (**Figs. S2a** to **S2c**). The calculated maximum spin temperatures (T_s^{max}, marked by blue stars) remain below the Curie temperature of Py (T_C = 800 K), which is consistent with our experimental observations of helicity non-switching behavior of the vortex in zero magnetic field, indicating that laser excitation ($\leqslant$19.5 mJ/cm^2) does not melt the spin configuration of the vortex into a random paramagnetic state above T_C. The calculated maximum spin temperatures (T_s^{max}) increase almost linearly with laser fluence, with an intercept at 300 K

in the absence of fs laser pulse excitation (**Fig. S2d**). Our simulations, with the selected reasonable parameters, are compatible with our experimental observations. In order to further scale the photothermal demagnetization curves $M_s(t)$ for varied laser fluences, we performed magnetometry measurements of high temperature magnetization $M_s(T)$ of a Py film in a saturating in-plane magnetic field ($H = 0.5$ T) and fitted $M_s(T)$ using a modified Bloch law (**Fig. S2e**):

$$\frac{M_s(T)}{M_s(0)} = 1 - \left(\frac{T}{T_C}\right)^{\alpha} \tag{S5}$$

where $M_s(0)$ is the spontaneous magnetization at absolute zero and α is a dimensionless exponent. Based on the time-dependent spin temperatures $T_s(t)$ solved previously by the 3TM, scaled photothermal demagnetization curves $M_s(t)$ can be obtained for the corresponding laser fluence (**Fig. S2f**).

As the spin temperature under laser excitation ($\leqslant 19.5$ mJ/cm^2) remains below T_C, the spin configuration of the vortex stays in an ordered state with a decreased amplitude of M_s immediately after laser pulse excitation. We can therefore directly incorporate photothermal demagnetization curves $M_s(t)$ into the LLG equation for dynamical micromagnetic simulations.

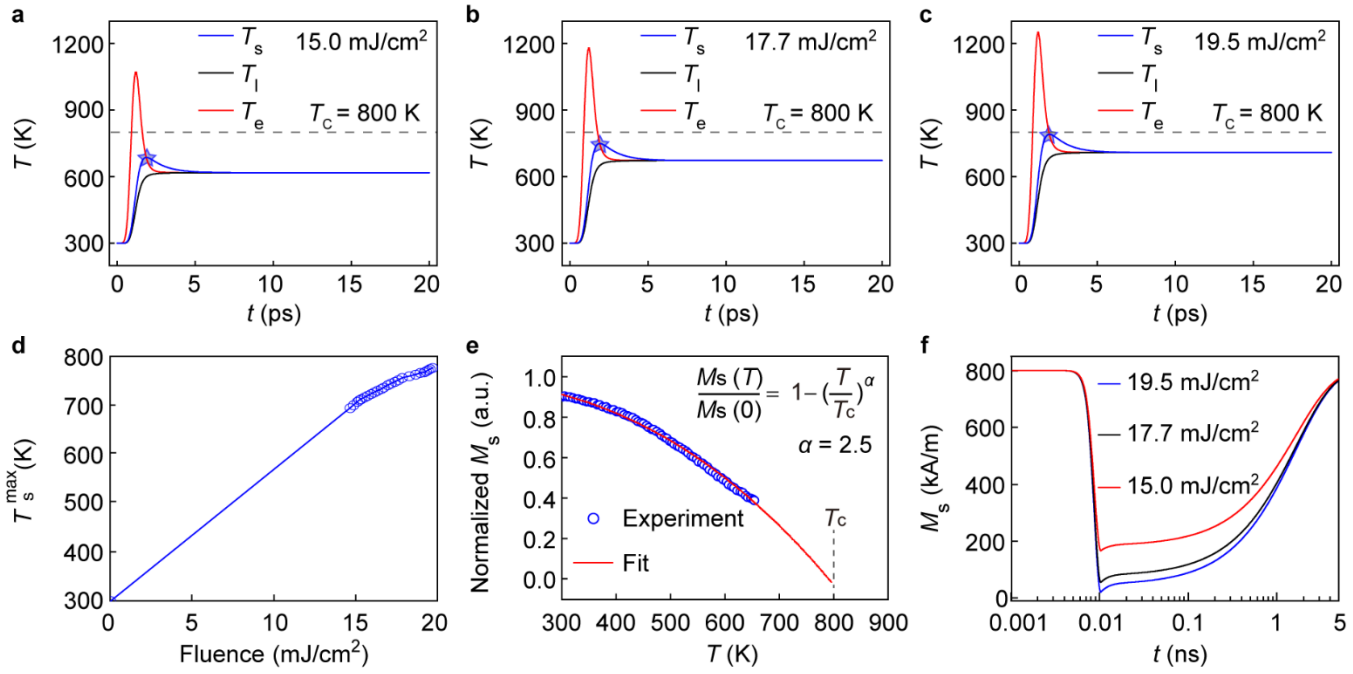

Fig. S2| a-c, Time-dependent temperatures of electrons (T_e), spins (T_s) and the lattice (T_l) calculated using the 3TM for laser fluences of between 15.0 and 19.5 mJ/cm^2. Blue stars mark the maximum spin temperatures (T_s^{max}) that remain below the Curie temperature of Py ($T_C = 800$ K, dashed line). **d,** Calculated T_s^{max} for varied laser fluences. **e,** Magnetometry measurement of high temperature magnetization $M_s(T)$ of a Py film in a saturating in-plane magnetic field ($H = 0.5$ T). **f,** Scaled photothermal demagnetization curves $M_s(t)$ for laser fluences of between 15.0 and 19.5 mJ/cm^2.

Note 2. Experimental observation of magnetic-field-dependent vortex helicity switching at a laser fluence of 19.5 mJ/cm^2

An *in situ* measurement result recorded at a laser fluence of 19.5 mJ/cm^2 is illustrated in **Fig. S3**. This figure depicts the calculated probabilities of helicity differences ($|\delta C| = 2,\ 1,\ 0$), which occur alternately as the out-of-plane magnetic field strength is increased. These probabilities were used to determine the expected values of $\langle|\delta C|\rangle$ shown in **Fig. 4a**. The dashed lines in **Fig. S3** represent three different types of helicity switching, as illustrated in **Figs. 2c** to **2e**.

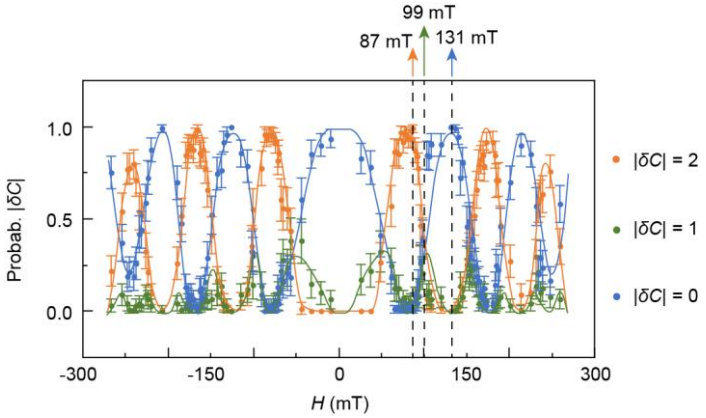

Fig. S3| Magnetic-field-dependent probabilities for different helicity switching behaviors ($|\delta C| = 2, 1, 0$) at a laser fluence of 19.5 mJ/cm^2. Data are presented as mean values with error bars representing the 95% CI, calculated assuming a binomial distribution. Data are presented as the probabilities of different types of helicity switching: $|\delta C| = 2$ (orange dots), $|\delta C| = 1$ (green dots), and $|\delta C| = 0$ (blue dots). The error bars represent two-sided 95% confidence intervals estimated using the normal approximation to the binomial distribution. Each data point is obtained from 100 repeated single-shot fs laser excitations (n = 100) applied to the magnetic vortex.

Note 3. Magnetic-field-dependent trajectory evolution of the magnetic vortex state on the Bloch sphere

In order to demonstrate the three distinct types of helicity switching behaviors ($|\delta C| = 2, 1, 0$), we illustrate the trajectory of the vortex state on the Bloch sphere for magnetic fields of 88, 100, and 126 mT under laser pulse excitation with a fluence of 19.5 mJ/cm^2. Coherent helicity switching ($|\delta C| = 2$) begins from an initial CW vortex state and undergoes a π rotation on the Bloch sphere to reach a final CCW vortex state (**Fig. S4a**). Helicity random switching ($|\delta C| = 1$) first involves a coherent $3\pi/2$-rotation to the topological critical point (TCP), and then drops into the inner space of the Bloch sphere, which corresponds to an incoherent process with formation of numerous vortex and antivortex defects (**Fig. S4b**).

Coherent helicity non-switching ($|\delta C| = 0$) circumnavigates the Bloch sphere with a 2π rotation to reach the initial CW vortex state (**Fig. S4c**).

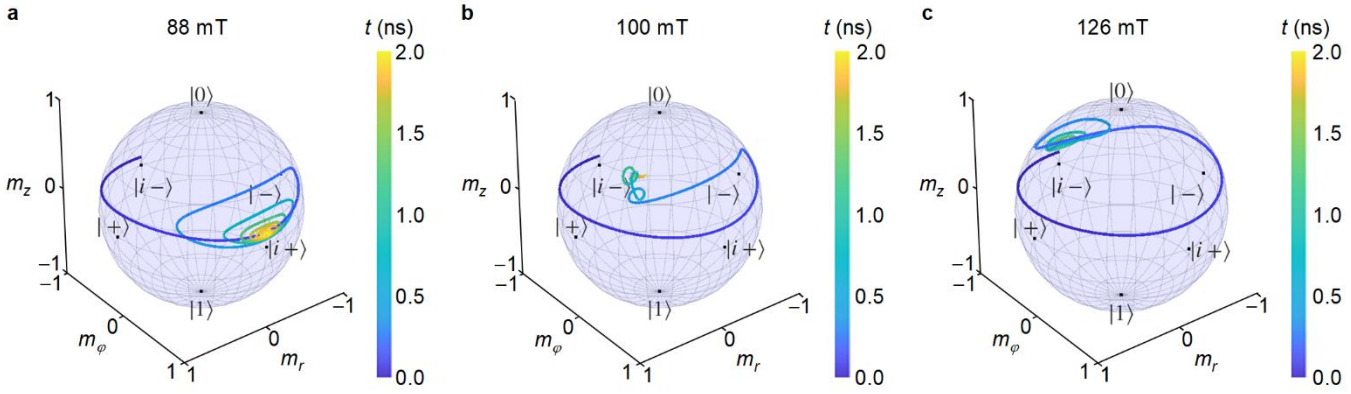

Fig. S4| a-c, Magnetic-field-tunable trajectory of the vortex state on the Bloch sphere for $H = 88$, 100 and 126 mT under a laser pulse excitation with a fluence of 19.5 mJ/cm^2. The color bar indicates the corresponding time scale for trajectory evolution of the vortex state.

Note 4. Magnetization dynamics in magnetic vortex in the coherent helicity non-switching process

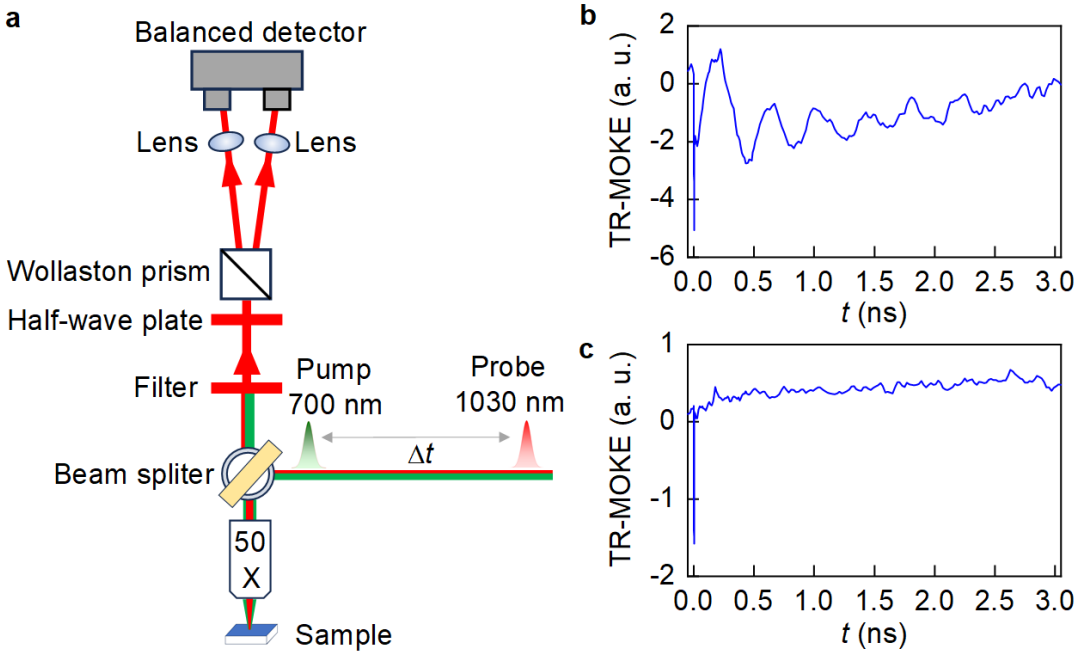

Fig. S5| Spin dynamics of the magnetic vortex under the helicity coherent non-switching process. a, Schematic diagram for the TR-MOKE experiment with a normal incident configuration. **b,** TR-MOKE experimental result of a typical helicity coherent non-switching process in a Py disk under a pump fluence of ~19.5 mJ/cm^2 within a perpendicular magnetic field of ~130 mT. **b,** TR-MOKE experimental result of a Py film without magnetic vortices under the same measurement conditions.

Because the helicity coherent non-switching is fully reversible and meets the pump-probe experimental requirement, we carried out pump-probe TR-MOKE measurement on the typical coherent helicity non-switching process in **Fig. 3e** under a pump fluence of ~19.5 mJ/cm^2 within the perpendicular field of ~130 mT, while the revealed underlying magnetization dynamics can also be generalized to case of the coherent helicity switching process. The TR-MOKE signal that reflects the temporal evolution of the space-averaged magnetization m_z in the vortex shows a periodic oscillation with time in the remagnetization process (**Fig. S5b**), which sustains a few nanoseconds with a gradual decrease in the oscillation amplitude. In contrast, the TR-MOKE result of a Py film with the same thickness under the similar condition exhibits no apparent oscillation (**Fig. S5c**) due to its soft magnetic nature without in-plane magnetic anisotropy and the absence of vortex sates. This dynamic feature further confirms the coherent magnetization precession dynamics of the vortex state in the helicity coherent non-switching process. Notice that, as demonstrated in the simulation results (**Figs. 3e**, **h** and **c** panel of **Supplementary Video 3**), although the precession dynamics of the global spins around their time-evolving effective fields may sustain a few nanoseconds, the switching forth and back of the helicity in the coherent non-switching process complete within ~450 ps, which is closely consistent with the duration (~440 ps) of the first oscillation with the largest amplitude in the TR-MOKE result (**Fig. S5b**). Combing this TR-MOKE result with the simulation results of the helicity coherent switching under a lower magnetic field (**Figs. 3c**, **f** and **a** panel of **Supplementary Video 3**), it is able to speculate that the helicity may finish the switching forth within ~270 ps, in which the magnetization precession has a lower frequency. These combined simulation and experimental results further indicate the ps-scale coherent nature of the magnetization dynamics in the helicity switching and non-switching processes.

Note 5. Experimental observation of magnetic-field-dependent vortex helicity switching at laser fluences of 17.7 and 15.0 mJ/cm^2

In addition to the vortex helicity switching behavior at a laser fluence of 19.5 mJ/cm^2 (**Fig. 2** in the main text), we performed *in situ* measurements at lower laser fluences of 17.7 and 15.0 mJ/cm^2 and determined phase diagrams for the helicity switching behaviors (**Figs. S6a** and **S6b**). By capturing Fresnel images using repetitive fs laser pulse excitations, the helicity difference $|\delta C|$ was determined by comparing vortex states before and after laser pulse excitation, where $|\delta C| = 2$ (white) indicates helicity reversal, $|\delta C| = 1$ (gray) indicates transitions between single core and multiple core vortices and $|\delta C| = 0$ (black) indicates no helicity change. The alternating black and white regions for varying magnetic fields correspond to transformations between different helicity switching behaviors. In order to further clarify these behaviors, **Figs. S6c** and **S6d** depict the calculated probability for the helicity differences ($|\delta C| = 2$, 1, 0), which are in turn used to determine the the expected values of $\langle|\delta C|\rangle$ given in the main text

(**Fig. 4a**).

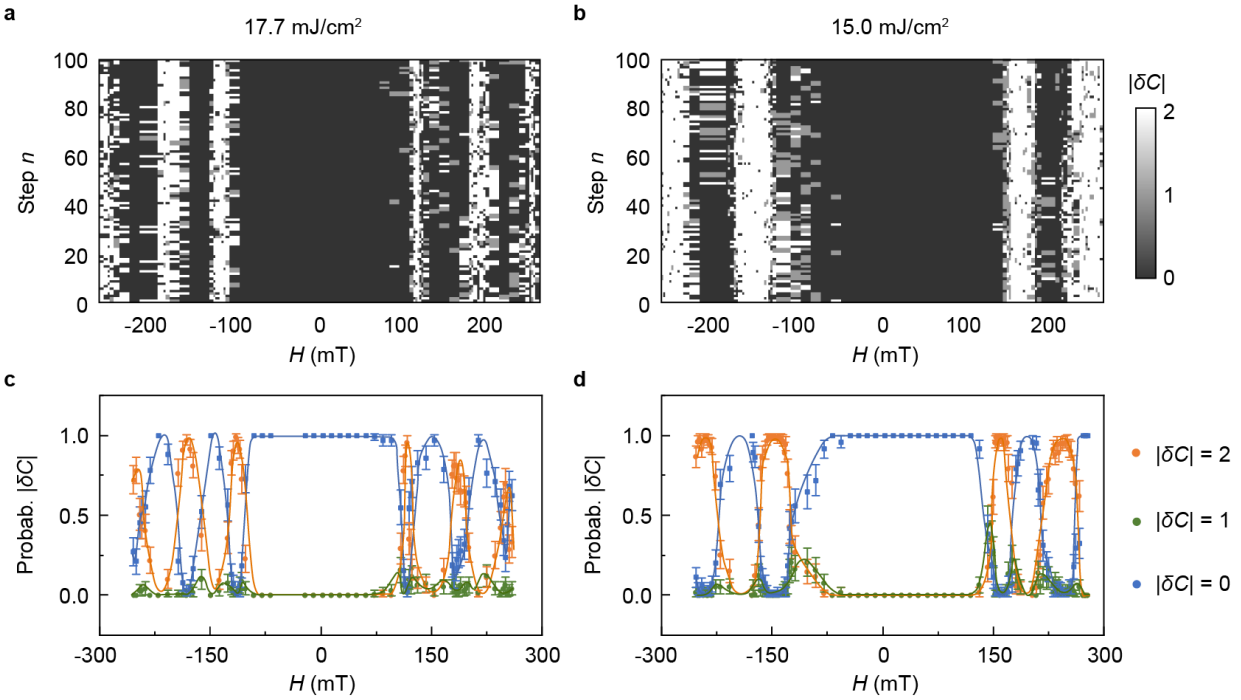

Fig. S6| a, b, Helicity switching of a vortex ($|\delta C|$) in varying magnetic fields over 100 continuous steps of fs laser pulse excitation at fluences of 17.7 and 15.0 mJ/cm^2, respectively. **c, d,** Probability of different helicity switching behaviors ($|\delta C| = 2$, 1, 0) at laser fluences of 17.7 and 15.0 mJ/cm^2, respectively. Data are presented as mean values with error bars representing the 95% CI, calculated assuming a binomial distribution. Data are presented as the probabilities of different types of helicity switching: $|\delta C| = 2$ (orange dots), $|\delta C| = 1$ (green dots), and $|\delta C| = 0$ (blue dots). The error bars represent two-sided 95% confidence intervals estimated using the normal approximation to the binomial distribution. Each data point is obtained from 100 repeated single-shot fs laser excitations ($n = 100$) applied to the magnetic vortex.

Note 6. Simulated magnetic-field-dependent vortex helicity switching at laser fluences of 17.7 and 15.0 mJ/cm^2

In addition to simulated field-dependent helicity switching process at a laser fluence of 19.5 mJ/cm^2 (**Fig. 3** in the main text), we performed numerical simulations for lower laser fluences of 17.7 and 15.0 mJ/cm^2 and determined phase diagrams of helicity angle $\sin(C\pi/2)$ as a function of magnetic field and time (**Fig. S7**). The initial CW vortex state (blue) undergoes l consecutive helicity reversals as the magnetic field is increased, where even values of l indicate helicity switching to a final CCW vortex state (red) and odd values of l indicate helicity non-switching to a final CW vortex state (blue). As the laser fluence is decreased, the simulated magnetic field required for helicity switching shifts to higher

values, in agreement with the experimental results shown in **Fig. S6**.

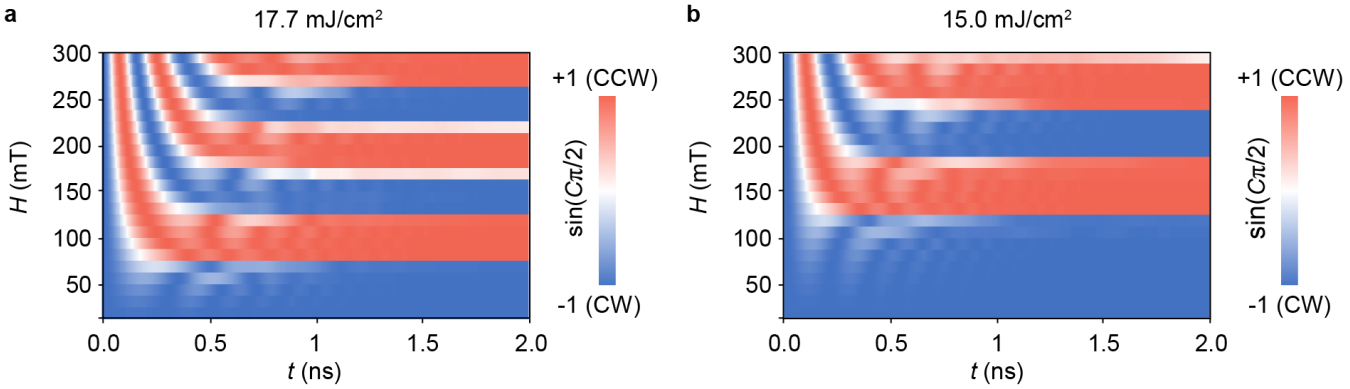

Fig. S7| a, b, Simulated time evolution of fs-laser-excited vortex helicity in varying magnetic fields for laser fluences of 17.7 and 15.0 mJ/cm^2, respectively. The blue color indicates a CW vortex state (C = -1) and the red color indicates a CCW vortex state (C = +1).

Note 7. Laser-fluence-dependent helicity switching of the magnetic vortex state

The laser-fluence-dependent alternating coherent helicity switching behavior is dominated by the ultrafast demagnetization process that reshapes the time evolution of the projected energy map on the Bloch sphere. The corresponding spin spatiotemporal evolution and time-dependent trajectory of the vortex state on the projected energy map of the Bloch sphere (H = 163 mT) are shown in **Figs. S8a** to **S8c**. At an excitation fluence of 14.5 mJ/cm^2 (**Fig. S8a**), the energy minimum points of the Bloch sphere shift slightly to a higher latitude and remain separated (0.05 ns) immediately after ultrafast photothermal demagnetization ($M_s(t)/M_s$ = 25%), and the initial CW vortex state starts a right-handed helix rotation from the left energy minimum point ($|\psi_{-1}\rangle$) on the Bloch sphere. Within a short time window (~150 ps), before the two energy minimum points recover to a lower latitude with a higher energy barrier, the trajectory of the vortex state completes a halfway rotation around the Bloch sphere. It is then rapidly trapped by the right energy minimum point ($|\psi_{+1}\rangle$) due to the higher energy barrier at ~0.2 ns, resulting in coherent helicity switching during the subsequent remagnetization process (see the left panel of **Supplementary Video 4** and **Fig. S9a**). For twice helicity reversals at a fluence of 16.3 mJ/cm^2, ultrafast photothermal demagnetization ($M_s(t)/M_s$ = 14%) drives the energy minimum points to the $|0\rangle$ pole point (0.05 ns) on the Bloch sphere, extending the time window (0.05-0.40 ns) for free circumnavigation of the vortex state trajectory before the energy minimum point separated with a high energy barrier (**Fig. S8b**). The trajectory of the vortex state can therefore circumnavigate the Bloch sphere and be re-trapped by the initial left energy minimum point ($|\psi_{-1}\rangle$), resulting in coherent helicity non-switching during the subsequent remagnetization process (see middle panel of **Supplementary Video 4** and **Fig. S9b**). At the

higher laser fluence of 19.5 mJ/cm^2, grater photothermal demagnetization ($M_s(t)/M_s = 3.5\%$) opens a longer time window (0.05-0.80 ns), which allows for further circumnavigation of the vortex state on the Bloch sphere (**Fig. S8c**), leading to three times vortex helicity reversals in this time window. The subsequent remagnetization process results in a vortex state with a switched helicity (0.80-2.00 ns; see right panel of **Supplementary Video 4** and **Fig. S9c**). All of these dynamical processes are coherent, as the temporal evolutions of their space-averaged magnetization components (m_r, m_φ and m_z) remain in phase with the modulus |**m**| unchanged (**Figs. S8d** to **S8f**). These results indicate that tuning of the laser fluence alone can also effectively control the coherent switching behavior of the vortex state without changing the external magnetic field.

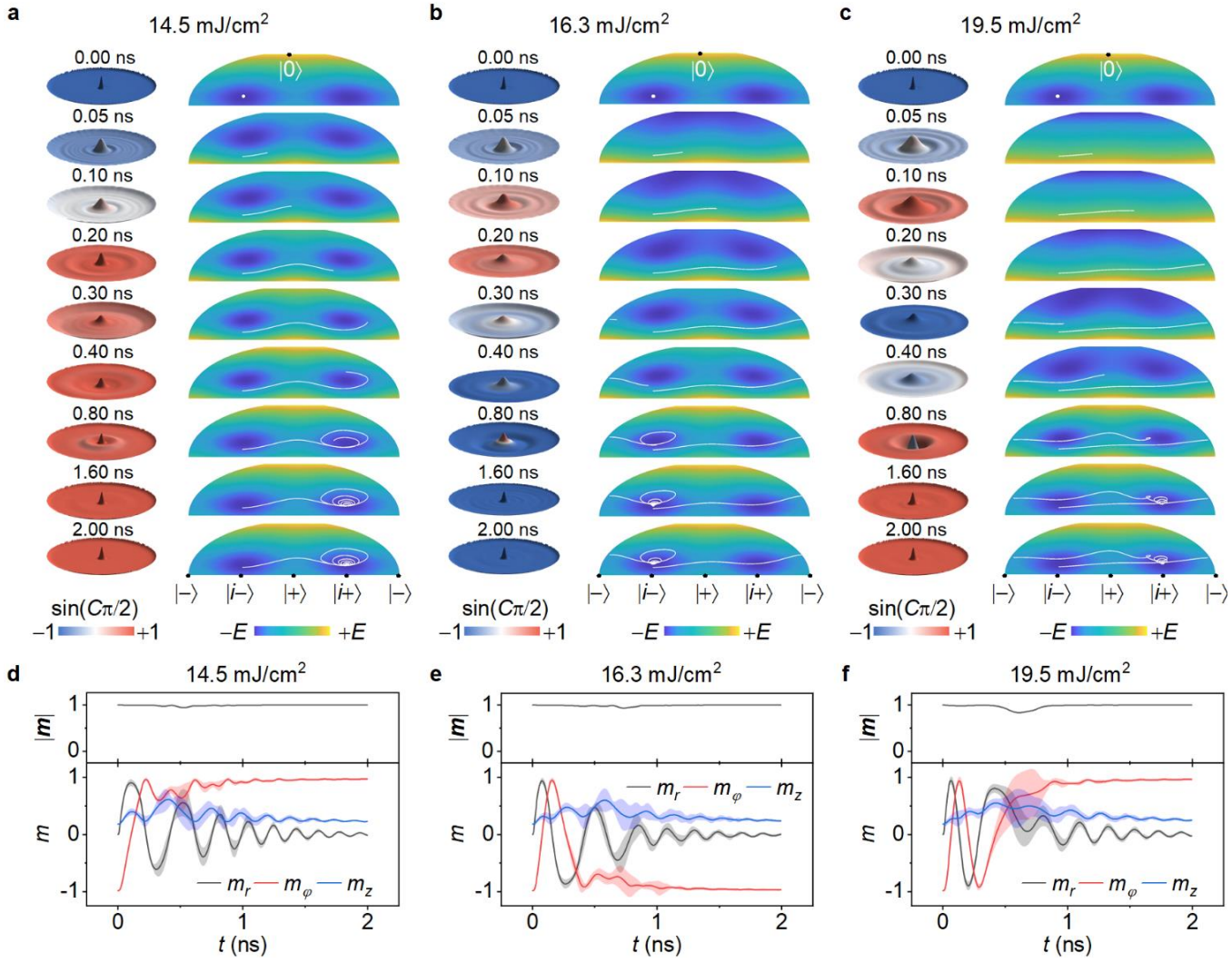

Fig. S8| a-c, Representative switching processes for π, 2π and 3π rotation of the helicity $\delta C\pi/2$ for three laser fluences (J = 14.5, 16.3 and 19.5 mJ/cm^2) in an out-of-plane magnetic field of H = 163 mT. Left panel: Snapshot of vortex helicity (blue/red) and m_z (height) distribution during helicity switching. Right panel: Energy map evolution in the Bloch vector representation, with the corresponding trajectory of the

vortex state (white) shown in the left panel. Blue indicates an energy minimum and yellow indicates an energy maximum. **d-f,** Corresponding time evolution of the space-averaged magnetization **m** and the corresponding modulus |**m**|. The error bars represent the standard deviation of the spatially averaged magnetization components calculated over all discretized simulation cells within the disk.

Note 8. Laser-fluence-dependent trajectory evolution of the magnetic vortex state on the Bloch sphere

In order to demonstrate the laser-fluence-dependent alternating coherent helicity switching behavior, the trajectory of the vortex state on the Bloch sphere is illustrated here for laser fluences of 14.5, 16.3 and 19.5 mJ/cm^2 in a fixed magnetic field of 163 mT (**Fig. S9**). The trajectory of vortex rotation follows a right-handed helix path, with the helicity angle progressing through π (14.5 mJ/cm^2), 2π (16.3 mJ/cm^2) and 3π (19.5 mJ/cm^2).

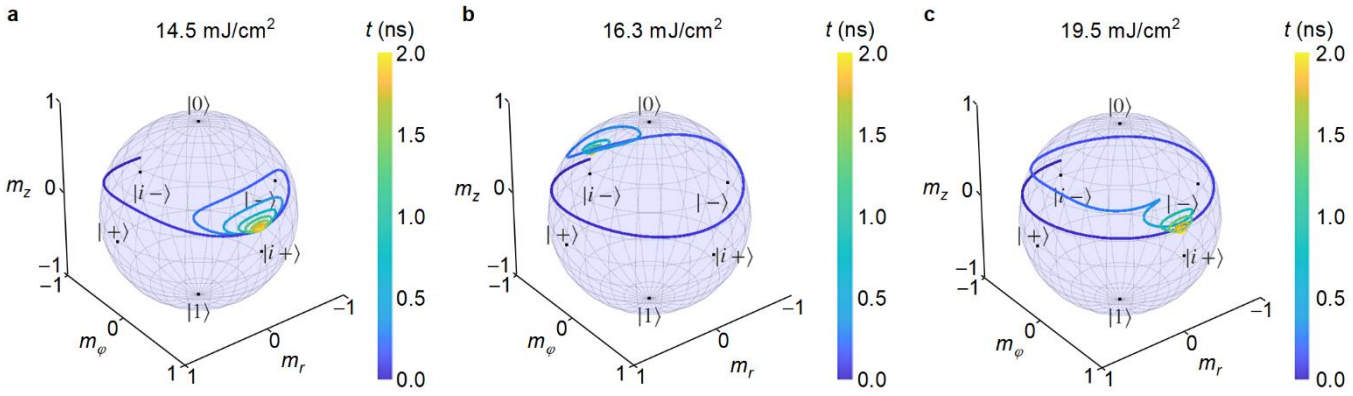

Fig. S9| a-c, Laser-fluence-tunable trajectory of the vortex state on the Bloch sphere for J = 14.5, 16.3 and 19.5 mJ/cm^2 in a fixed magnetic field of 163 mT. The color bar indicates the corresponding time scale for trajectory evolution of the vortex state.

Note 9. A possible strategy for mimicking single qubit operation based on ultrafast coherent switching of topological spin helicity

It has been theoretically proposed that coherently controllable helicity switching of topological swirling spin configurations hold potential for mimic quantum logic operation by encoding the superposition state ($|\psi_C\rangle$) of the two energy-degenerate CW ($|i\text{-}\rangle$) and CCW ($|i\text{+}\rangle$) helicity states on the Bloch sphere representation [8-12]. Therefore, our experimental realization of coherent helicity switching in the magnetic vortex system may also provide a way for mimicking single qubit operation at room

temperature by encoding the superposition state of its two energy-degenerate helicity states on the Bloch sphere. The mimicking of such single qubit operation could be achieved by precisely controlling the arbitrary rotation trajectory of the vortex state on the Bloch sphere using a combination of an out-of-plane magnetic field and a fs laser pulse. For example, by adjusting the magnetic field strength or the laser fluence, coherent magnetization precession can be controlled to achieve l times intermediate helicity reversal (left and middle panels of **Fig. S10a**), where odd and even values of l correspond to helicity switching and helicity non-switching with 100% probability, respectively. Furthermore, by implementing an excitation $\hat{U}(t)$ with a tuned magnetic field strength and laser fluence, the rotation of an initially CCW state ($|i+\rangle$) to an arbitrary superposition state on the Bloch sphere can be described as $\hat{U}(t)|i+\rangle = \alpha|i+\rangle + \beta|i-\rangle$, where the probability amplitudes α and β are complex numbers and the probabilities P of measuring a final vortex state $|i+\rangle$ and $|i-\rangle$ are $|\alpha|^2$ and $|\beta|^2$, which are normalized so that $|\alpha|^2 + |\beta|^2 = 1$ (right panel of **Fig. S10a**). The single qubit operations mimicked with a topologically-protected magnetic vortex offers an inherent advantage of easy initialization and a significantly long lifetime (left panel of **Fig. S10b**). In addition, quantum computation simulation can be performed by using sequenced excitations $\hat{U}(t)$ with the combined use of out-of-plane magnetic fields and fs laser pulses (middle panel of **Fig. S10b**), and readout can be achieved by measuring the probability of the resulting vortex states (right panel of **Fig. S10b**). As a result, the probabilities $|\alpha|^2$ and $|\beta|^2$ would oscillate with increasing magnetic field or laser fluence (**Fig. S10c**), as also demonstrated by our *in situ* experiments (**Figs. 2c** to **2e**, **Supplementary Information Section 5** and **Fig. 4a**) and theoretical simulations (**Fig. 4b** and **Supplementary Information Section 6**). As topological protection of the magnetic vortex states ensures stability against external perturbations, making them as potential candidates for mimicking low-error quantum computation at room temperature.

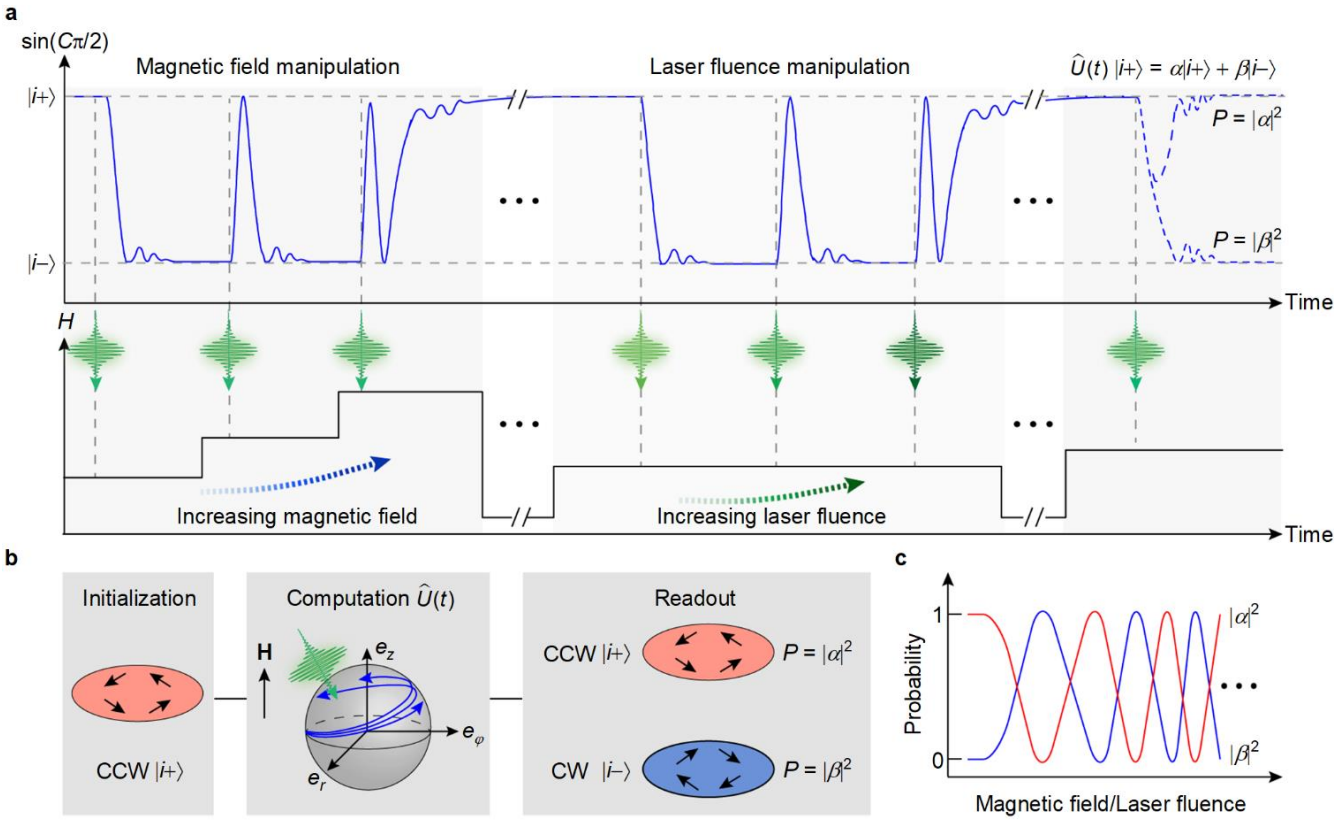

Fig. S10| Single qubit design and operation based on ultrafast coherent switching of topological spin helicity. a, Schematic diagrams of magnetic vortex qubit operations $\hat{U}(t)|i+\rangle = \alpha|i+\rangle + \beta|i-\rangle$ realized by implementing an excitation $\hat{U}(t)$ with a tuned magnetic field strength (left panel) and laser fluence (middle panel), illustrating helicity non-switching and switching with tunable probabilities of $|\alpha|^2$ and $|\beta|^2$ (right panel). **b,** Flowchart of single qubit design for initialization with a CCW vortex state (left panel), computation with field-assisted laser excitation (middle panel) and readout by measuring the probability of the final CCW or CW vortex state (right panel). **c,** Oscillations in helicity switching probability plotted as a function of magnetic field or laser fluence.

Note 10. The parameters used for calculating laser fluence

The parameters used for calculating laser fluence are listed in **Table S2**. The laser fluence J (in mJ/cm^2) is determined using the following equation:

$$J = \frac{P}{f \times S} \tag{S6}$$

where P is the laser power (mW), f is the repetition rate (Hz), and S is the laser spot area (cm^2).

Table S2| The parameters used for calculating laser fluence.

Parameter	Value	Unit
Laser power	2.2/2.0/1.7	mW
Diameter of spot size	~120	μm
Frequency	1	kHz
Fluence	19.5/17.7/15.0	mJ/cm^2

References

1. Kirilyuk, A., Kimel, A. V. and Rasing, T. Ultrafast optical manipulation of magnetic order. *Rev. Mod. Phys.* **82**, 2731-2784 (2010).
2. Beaurepaire, E., Merle, J. C., Daunois, A. *et al.* Ultrafast spin dynamics in ferromagnetic nickel. *Phys. Rev. Lett.* **76**, 4250-4253 (1996).
3. Alber, L., Scalera, V., Unikandanunni, V. *et al.* NTMpy : An open source package for solving coupled parabolic differential equations in the framework of the three-temperature model. *Comput. Phys. Commun.* **265**, 107990 (2021).
4. Fu, X., Pollard, S. D., Chen, B. *et al.* Optical manipulation of magnetic vortices visualized in situ by Lorentz electron microscopy. *Sci. Adv.* **4**, eaat3077 (2018).
5. Ellis, M. O. A., Ostler, T. A. and Chantrell, R. W. Classical spin model of the relaxation dynamics of rare-earth doped permalloy. *Phys. Rev. B* **86**, 174418 (2012).
6. Mukhopadhyay, S., Majumder, S., Narayan Panda, S. *et al.* Investigation of ultrafast demagnetization and Gilbert damping and their correlation in different ferromagnetic thin films grown under identical conditions. *Nanotechnology* **34**, 235702 (2023).
7. Panda, S. N., Mondal, S., Majumder, S. *et al.* Ultrafast demagnetization and precession in permalloy films with varying thickness. *Phys. Rev. B* **108**, 144421 (2023).
8. Psaroudaki, C. and Panagopoulos, C. Skyrmion qubits: a new class of quantum logic elements based on nanoscale magnetization. *Phys. Rev. Lett.* **127**, 067201 (2021).
9. Psaroudaki, C. and Panagopoulos, C. Skyrmion helicity: quantization and quantum tunneling effects. *Phys. Rev. B* **106**, 104422 (2022).
10. Xia, J., Zhang, X., Liu, X. *et al.* Universal quantum computation based on nanoscale skyrmion helicity qubits in frustrated magnets. *Phys. Rev. Lett.* **130**, 106701 (2023).
11. Psaroudaki, C., Peraticos, E. and Panagopoulos, C. Skyrmion qubits: Challenges for future quantum computing applications. *Appl. Phys. Lett.* **123**, 260501 (2023).
12. Pan, X.-F., Hei, X.-L., Yao, X.-Y. *et al.* Skyrmion-mechanical hybrid quantum systems: Manipulation of skyrmion qubits via phonons. *Phys. Rev. Res.* **6**, 023067 (2024).